Journal of Computational Physics 448 (2022) 110755

Contents lists available at ScienceDirect

Journal of Computational Physics

www.elsevier.com/locate/jcp

Conservative finite volume method on deforming geometries: The case of protein aggregation in dividing yeast cells

A. Ali Heydari [a,b], Suzanne S. Sindi [a,b], Maxime Theillard [a,*]

[a] Department of Applied Mathematics, University of California, Merced, CA 95343, USA
[b] Health Sciences Research Institute, University of California, Merced, CA 95343, USA

ARTICLE INFO

Article history:
Available online 7 October 2021

Keywords:
Conservative
Finite volume
Level set
Octree
Protein aggregation
Dividing cell

ABSTRACT

Motivated by experimental observations of asymmetric protein aggregates distributions in dividing yeast cells, we present a conservative finite volume approach for reaction-diffusion systems defined over deforming geometries. The key idea of our approach is to use spatio-temporal control volumes instead of integrating the time-discretized equations in space, as it is common practice. Both our theoretical and computational results demonstrate the convergence of our method and highlight how traditional approaches can lead to inaccurate solutions. We employ this novel approach to investigate the partitioning of protein aggregates in dividing yeast cells, leveraging the flexibility of the level set method to construct realistic biological geometries. Using a simple reaction-diffusion model, we find that spatial heterogeneity in yeast cells during division can alone create asymmetries in the concentration of protein aggregates. Moreover, we find that obstructing intracellular entities, such as nuclei or insoluble protein compartments, amplify these asymmetries, suggesting that they may play an essential role in regulating molecular partitioning. Beyond these findings, our results illustrate the flexibility of our approach and its potential to design realistic predictive tools to explore intracellular bio-mechanisms.

1. Introduction

Cells are often considered to be the smallest unit of life because they group critical constituents within a single compartment. Inside the boundary of a cell, the environment is continually changing as molecular species are constantly created, degraded, and interacting with one another [35]. Mathematical models have proven to be powerful tools in biology through their ability to provide abstract representations of the cellular environment, generate simulations under distinct hypotheses, provide quantitative output that can be validated through comparisons with experiments [41,42]. However, mathematical modeling necessarily involves making simplifying assumptions about both the cell itself and its environment.

One common assumption is that the cell environment is well-mixed and spatially homogeneous, allowing for the use of deterministic ordinary differential equations or stochastic simulations of the chemical master equation, which offer both analytical and computational advantages over their partial differential equation counterparts [3,55,12,31]. However, even if the cell began as a well-mixed compartment, reaction, diffusion, and cellular reconfiguration can create spatial heterogeneities, which may cause unequal partitioning after cellular division [15,53]. More recently, structured population equations have proven useful to consider populations of cells where intracellular constituencies may be partitioned unequally [53,28].

* Corresponding author.
E-mail address: mtheillard@ucmerced.edu (M. Theillard).

https://doi.org/10.1016/j.jcp.2021.110755

However, these models still rely on the assumption that within individual cells, the environment is well-mixed. With the increasing ability to experimentally observe distributions of biochemical species within individual cells, it becomes necessary to favor mathematical methods which model spatial heterogeneity. For such a model to be realistic, it must reproduce observed cell deformations while preserving essential physical properties such as mass conservation.

Over the last decades, the level set method [47,52] has been recognized as a versatile interface representation, virtually applicable to any interfacial problem. The interface is defined as the zero contour of a continuous function (*i.e.* the level set function), and an advection equation models its evolution. Doing so, the costly mesh conformation, inherent to any method explicitly tracking the geometry, is replaced by the numerical resolution of a standard partial differential equation. The level set method has been employed to simulate a broad range of applications in computer, engineering, and natural sciences, such as the dynamic multi-phase flows [59], the electrostatic of biomolecules [40], or the response of elastic structures [57]. In computational biology, it has for example been used to simulate the behavior of self-healing [64], growing [4] and shear stress-stimulated [24,25] tissues, tumor growth [34,67,48], wound healing [29] or the protrusion of cells in micropipettes [69]. Even though the level set formalism seems to be the natural mathematical tool for studying the dynamics of single cells, to the best of our knowledge, it has not been used to study protein aggregation in three-dimensional yeast cells.

In this work, we present a framework for studying the reaction-diffusion process in deforming cells and employ it to simulate prions aggregation in dividing yeast cells. First, we construct a level-set based model to represent the budding cell cycle of yeasts; that is, our model begins with a single compartment (mother cell), which through the budding processes, produces a growing daughter cell that ultimately disconnects completely (see Fig. 2). Second, we construct a novel finite volume formulation that ensures mass conservation even on deforming geometries. Third, we validate our model using analytical and practical examples and finally employ it to study the impact of intracellular material and biochemistry on the prions transmission process. Our results both illustrate the limitations of the well-mixed assumptions and the ability of the reaction-diffusion mechanisms to create asymmetric distribution alone. In addition to providing insights into the segregation of proteins in yeast, our work demonstrates the ability of our framework to serve as a tool for modeling cell division and intracellular dynamics providing a powerful testbed for mathematical biologists to generate predictions on an increasingly relevant experimental scale.

We start in Section 2 by providing background for our biological motivations. In Section 3 we describe our mathematical model, both the reaction-diffusion system and the level set representation. We then introduce our conservative finite volume formulation in section 4 and validate it in section 5. We apply our framework to simulate prions dynamics in dividing yeast cell in Section 6 and conclude in Section 7.

2. Biological background

2.1. Proteins aggregation and prions diseases

Proteins are linear sequences of amino acids, which then fold into a three dimensional shape or conformation. The function of a protein is tightly connected to its conformation [1]. As such, cells have a developed a protein-quality control mechanisms, including molecular chaperones, which degrade misfolded or damaged proteins [13]. Prions are a special class of proteins which are capable of adopting multiple stable conformations, which not only fail to be removed by protein quality control mechanisms, but which themselves can induce proteins in the normal confirmation to change to the alternate (prion) conformation [62].

More specifically, the proteins in the prion conformation form aggregates. These aggregates then convert normally folded protein to the prion state by acting as a template. The newly misfolded protein monomer then is incorporated into the aggregate, thus increasing its size. Then, rather than be cleared by protein quality control mechanisms, these aggregates can be split (fragmentation), which then increases both the number of aggregates and rate of further misfolding [62].

In mammals, prions have only been associated with progressive, untreatable and fatal neurodegenerative disease [32,49]. Prions disease in mammals can be infectious between members of the same species (scrapie in sheep, kuru in humans), occur spontaneously in an individual (Creutzfeldt-Jakob disease and fatal familial insomnia, and can even jump between species as when humans acquire variant Creutzfeldt-Jakob disease from consuming meat from cattle with bovine spongiform encephalopathy (Mad Cow disease) [20]. Fortunately, in humans prion diseases are rare. There are less than 400 reported cases of Creutzfeldt-Jakob disease per year, but approximately 70% of those affected die within a year of exposure [44]. Fatal familial insomnia, though rare, is typically fatal within only 18 months of initial symptoms [7].

While prion diseases are rare, the biochemical processes of prion disease are closely related to other protein misfolding diseases such as Alzheimer's and Parkinson's diseases. All these diseases are related by the common amyloid structure of their corresponding protein aggregates. As such, much of the research within the prion disease aims to characterize the dynamics of the amyloid protein aggregates which will provide insights into classes of much more common disease [20,26]. Much of the research within the field aims to characterize the dynamics of protein aggregates that cause prion and amyloid diseases [20,26]

One powerful biological tool for studying prion and protein aggregation processes is the single-celled yeast *Saccharomyces cerevisiae* (see Fig. 1). However, because yeast cells are quite different from mammalian cells, mathematical models of protein aggregation in yeast need to include different processes from those models designed for mammals.

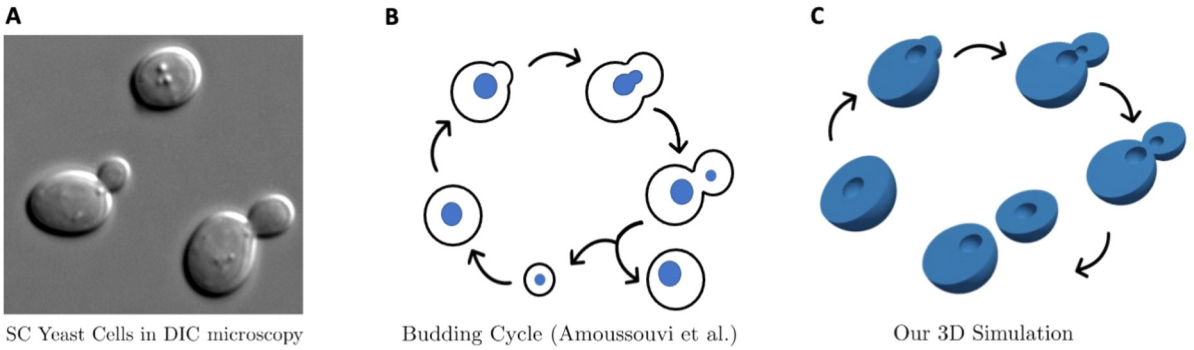

Fig. 1. Asymmetric yeast cell division. **A** Saccharomyces cerevisiae yeast cells under Differential Interference Contrast (DIC) microscopy showing two yeast cells (at the bottom) budding [14]. **B** Illustration of a yeast cell budding, as depicted by Amoussouvi et al. [5]. **C** Half space rendering of our three-dimensional simulation of single yeast cell budding.

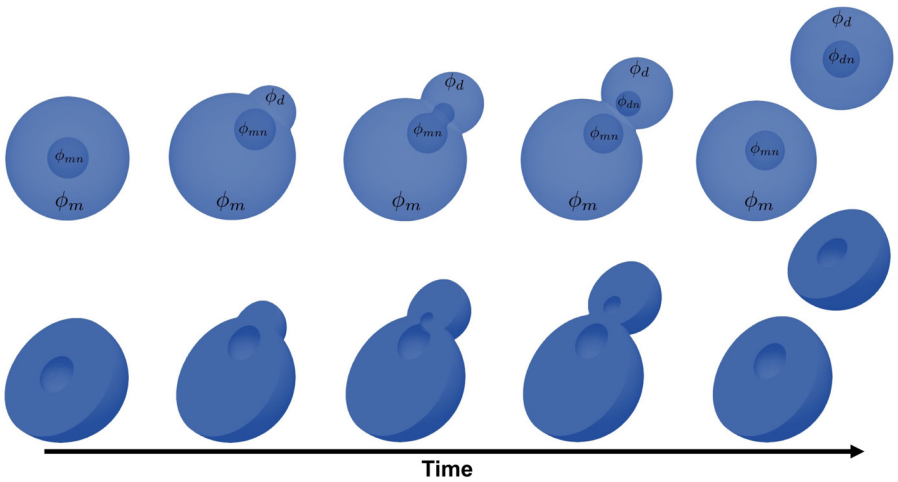

Fig. 2. Top row: full three-dimensional simulation of a yeast cell (larger sphere ϕ_m) with its nucleus (the middle sphere ϕ_{mn}) at its center. As time progresses, the daughter cell, ϕ_d, and its nucleus, ϕ_{dn} starts budding off. **Bottom row**: half space rendering of the yeast cell budding.

2.2. Yeast cells and asymmetric division

The single-celled yeast *Saccharomyces cerevisiae* has emerged as a model eukaryote in biological research and, as such, is the subject of our study. Yeast biologists have a host of experimental manipulations at their disposal, making yeast an ideal system to study a host of biological processes including protein misfolding and aging [10,62,50].

Yeast are an attractive system for studying protein misfolding because, unlike for mammals, protein misfolding in yeast is not fatal or harmful. Moreover in yeast, also unlike mammals protein misfolding processes can be turned on and off [21,51,16]. That is, protein misfolding can be reliably induced in healthy cells [17] and, for certain protein mutants, protein misfolding phenotypes can be destabilized (i.e., all of the misfolded protein will return to normal.) There are even studies which indicate misfolded protein aggregates may have benefits for yeast [43]. However, yeast are useful tools for biological questions in other areas.

The cell-division process in yeast makes them a valuable tool for studying aging. Unlike bacteria, which divide into two identical (or nearly identical) cells, yeast divide asymmetrically through budding into a mother cell and a daughter cell (see Fig. 2). In budding cell division, a new (daughter) cell is grown as an outgrowth of the old (mother) cell. At the time of separation, the mother cell is larger than the daughter cell. Finally, the daughter does not inherit the replicative age of the mother [27]. Although intracellular constituencies, including the nucleus, are transmitted from mother to daughter cell through a narrow bud neck connecting them, not all constituents transmit with equal efficiencies. Mother cells have been shown to preferentially retain a variety of “damaged” protein species, and this bias in retention can not be explained by differences in volume [68].

Intriguingly, prion aggregates are one such cellular constituency that has been shown to not transmit efficiently between mother and daughter cells [21]. A variety of theories have emerged to explain this bias: (1) Misfolded proteins are larger and therefore less mobile, especially in a crowded environment such as the intracellular matrix, and therefore have a harder progressing toward the daughter cell; (2) “Chaperones” proteins are present in the cell and forcibly restrict the damaged proteins to particular compartments, preventing them from reaching the daughter cell. These two assumptions can be

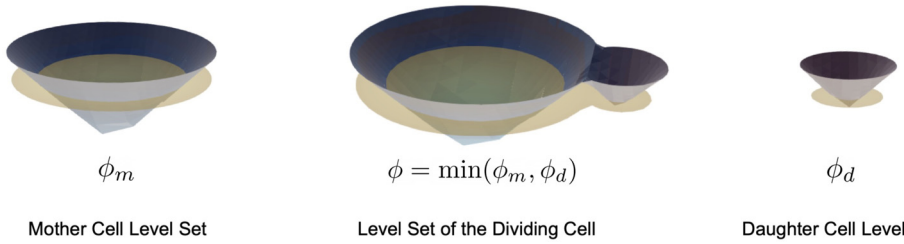

Fig. 3. Level set representation of a dividing yeast cell in two-dimensions: the beige plane depicts the zero level set, and the three-dimensional surface illustrates the level set functions of mother and daughter cells (that are in two-dimensions), denoted by ϕ_m and ϕ_d respectively. The union of the two biological cells is reproduced by taking the minimum of their level set function.

respectively seen as passive and active cellular. The mathematical modeling framework we propose offers the capability to investigate these causes. However, for the present scope, we will focus on the passive assumptions alone.

3. Biological modeling

Our mathematical model is built as a two-species reaction-diffusion system defined over a deforming geometry, itself represented by a level set function. To study the influence of intracellular compartments, we will consider a succession of geometries with increasing complexity and discuss their construction.

3.1. Governing equations

We consider two protein species, A and B, living inside a deforming cell $\Omega(t)$ (see Fig. 2), and track their respective concentrations ψ_A and ψ_B. We assume that A is a monomer, and that it can aggregate with itself to form the dimer B, which itself can degrade into two monomers. We define the dimerization and degradation rate as γ_{AB} and γ_{BA} respectively. Additionally, both species are diffusing with the corresponding diffusivities D_A and D_B. The concentrations ψ_A and ψ_B are therefore solutions of the reaction-diffusion equations

$$\frac{\partial \psi_A}{\partial t} - D_A \triangle \psi_A = 2\gamma_{BA}\psi_B - \gamma_{AB}\psi_A^2 \qquad \forall \mathbf{x} \in \Omega(t), \tag{1}$$

$$\frac{\partial \psi_B}{\partial t} - D_B \triangle \psi_B = \frac{1}{2}\gamma_{AB}\psi_A^2 - \gamma_{BA}\psi_B \qquad \forall \mathbf{x} \in \Omega(t). \tag{2}$$

We assume the cell membrane to be hermetic, and therefore enforce a no-flux boundary condition on the contour of the cell $\partial\Omega(t)$

$$\nabla \psi_A \cdot \mathbf{n} = 0 \quad \forall \mathbf{x} \in \partial\Omega(t), \tag{3}$$

$$\nabla \psi_B \cdot \mathbf{n} = 0 \quad \forall \mathbf{x} \in \partial\Omega(t), \tag{4}$$

where $\mathbf{n}$ denotes the normal vector to $\partial\Omega(t)$.

3.2. Level set representation

For the biological motivation, we construct $\Omega(t)$, the inside of the dividing yeast cell, by decomposing it into multiple subdomains (see Fig. 2). To each subdomain, we associate a level set function. Then, as illustrated in Fig. 3, we assemble the complete geometry by taking unions and intersections of these subdomains, which is equivalent to taking min and max of the corresponding level set functions.

This setup allows us to construct a succession of four geometrical representations of increasing complexity to evaluate the impact of each geometrical feature on the prion aggregation problem. From the initial representation containing the mother ϕ_m and daughter ϕ_d cells only (Fig. 4-A), we successively introduce the mother nucleus ϕ_{mn} (Fig. 4-B), the daughter nucleus ϕ_{dn} (Fig. 4-C), and finally two compartments found in yeast cells, the JUNQ (juxtanuclear quality control compartment) and IPOD (Insoluble Protein Deposit) [30] (Fig. 4-D). We will use the convention that the level set function is negative inside the domain of interest.

A No Nuclei

In this first case, we represent the dividing mother cell as the stationary domain Ω_m and its detaching daughter cell $\Omega_d(t)$ as two spheres represented by the following level set functions

$$\phi_m(\mathbf{x}, t) = |\mathbf{x} - \mathbf{x}_m| - r_m, \tag{5}$$

$$\phi_d(\mathbf{x}, t) = |\mathbf{x} - \mathbf{x}_d(t)| - r_d(t), \tag{6}$$

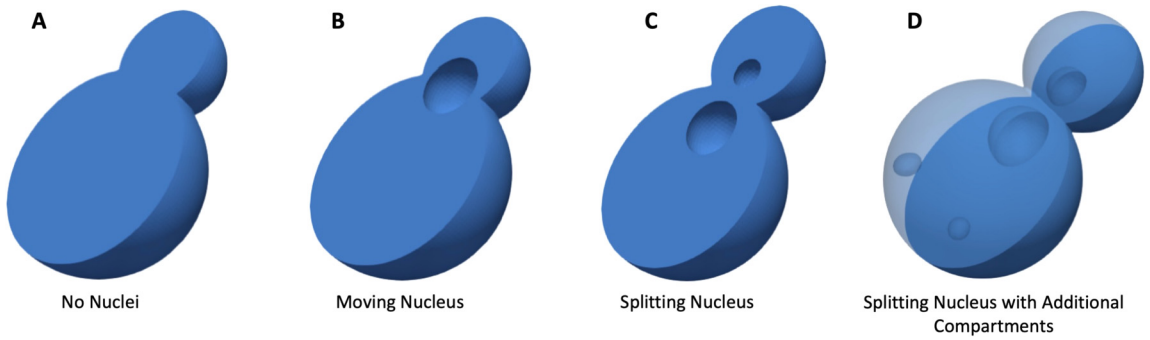

Fig. 4. Succession of geometric representations: we start by modeling the cell budding of the mother cell without any nucleus **A**. Then, we introduce a moving nucleus as shown in **B**, allow the nucleus to split **C**m and finally consider additional moving compartments in the mother cell **D**. We describe the specifics of the geometry for our problem in Section 3.2.

where $\mathbf{x}_m$ and $\mathbf{x}_d(t)$ are the center of the mother and daughter cell and r_m and $r_d(t)$ are the respective radii. The entire dividing cell is defined as the union of these two domains and is represented by the level set function $\phi = \min(\phi_m, \phi_d)$, as Fig. 3 illustrates.

B Moving Nucleus

Similarly we define the center $\mathbf{x}_{mn}(t)$ of the nucleus of the mother cell, its radius $r_{mn}(t)$ and corresponding level set function

$$\phi_{mn}(\mathbf{x}, t) = |\mathbf{x} - \mathbf{x}_{mn}(t)| - r_{mn}(t). \tag{7}$$

The upgraded domain $\Omega(t)$ over which the governing equations are valid is now the intersection of previous domain with the outside of the mother nucleus

$$\Omega(t) = (\Omega_m \cup \Omega_d(t)) \cap \Omega_{mn}^c(t), \tag{8}$$

or equivalently in terms of the level set functions

$$\phi = \max(\min(\phi_m, \phi_d), -\phi_{mn}). \tag{9}$$

C Splitting Nucleus

Following case (i), we define a new level set function for the daughter's nucleus, which we model detaching from the mother cell's nucleus, as it is observed in nature. The corresponding level set function is

$$\phi_{dn}(\mathbf{x}, t) = |\mathbf{x} - \mathbf{x}_{dn}(t)| - r_{mn}(t) - r_{dn}(t), \tag{10}$$

leading to

$$\Omega(t) = (\Omega_m \cup \Omega_d(t)) \cap (\Omega_{mn}(t) \cup \Omega_{dn}(t))^c \quad \Longleftrightarrow \quad \max(\min(\phi_m, \phi_d), -\min(\phi_{mn}, \phi_{dn})) \tag{11}$$

D Additional Cellular Compartments (IPOD and JUNQ)

Finally for our most comprehensive model we include two cellular compartments representing Insoluble Protein Deposit (IPOD) and Juxta Nuclear Quality (JUNQ); we describe the rolls of IPOD and JUNQ in prion aggregation later. We model these compartments as moving and rotating ellipsoids of centers $\mathbf{x}_I(t), \mathbf{x}_J(t)$ and parameters $\mathbf{p}_I(t), \mathbf{p}_J(t)$

$$\phi_I(\mathbf{x}, t) = \left(\left(\frac{(x - x_I(t))}{p_I^x(t)} \right)^2 + \left(\frac{(y - y_I(t))}{p_I^y(t)} \right)^2 + \left(\frac{(z - z_I(t))}{p_I^z(t)} \right)^2 \right)^{\frac{1}{2}} - 1, \tag{12}$$

$$\phi_J(\mathbf{x}, t) = \left(\left(\frac{(x - x_J(t))}{p_J^x(t)} \right)^2 + \left(\frac{(y - y_J(t))}{p_J^y(t)} \right)^2 + \left(\frac{(z - z_J(t))}{p_J^z(t)} \right)^2 \right)^{\frac{1}{2}} - 1. \tag{13}$$

The final geometry and level set function are

$$\Omega(t) = (\Omega_m \cup \Omega_d) \cap (\Omega_{mn} \cup \Omega_{dn})^c \cap \Omega_I^c \cap \Omega_J^c \qquad \forall \mathbf{x} \in \mathbb{R}^3, \forall t \geq 0, \tag{14}$$

$$\phi = \max\left(\min(\phi_m, \phi_d), -\min(\phi_{mn}, \phi_{dn}), -\phi_I, -\phi_J\right) \tag{15}$$

In our implementation we use the above formulas to initialize at each iteration the level set function, which we then reinitialize by reaching the steady state of the following equation

$$\frac{\partial \phi}{\partial \tau} + \text{sign}(\phi_0)\,(|\nabla \phi| - 1) = 0, \tag{16}$$

defined in fictitious time τ and over the entire computational domain. This is achieved using the second-order Total Variation Diminishing algorithm detailed in [39].

4. Numerical methods

This section presents our novel finite volume method and compares it to the traditional finite volume method, focusing, in particular, on mass conservation. While we will limit our analysis to the reaction-diffusion system describe in the above section, we should point out that it can easily be extended to other systems of partial differential equations. The last part of this section focus on the use and construction of adaptive non-graded octree grids.

4.1. Finite volume approach

The numerical solution of the system (1)-(2)-(3)-(4) is constructed using a semi-implicit finite volume method [36], which final form is given by Eqs. (35) and (36). The diffusive effects are treated implicitly for stability, while the non-linear reactive terms are treated explicitly. All diffusive fluxes are approximated using the second-order antisymmetric discretization proposed by Lossaso et al. [33] and used in our previous studies [23,61,9,59,56].

4.1.1. Notations, approximations, and remarks

All quantitites are stored at the centers of the octree grids. The control volumes V_i^n are defined as the intersection of the i^{th} computational cell C_i with the biological complex Ω^n at time step t^n (see Fig. 5)

$$V_i^n = C_i \cap \Omega^{n+1}. \tag{17}$$

The integrals over these volumes for any cell-based quantity q are approximated using the approximations

$$\int_{V_i^n} f = f_i |V_i^n| + \mathcal{O}(\Delta x^3). \tag{18}$$

The contour integrals of the normal fluxes $\nabla q \cdot \mathbf{n}$ over ∂V_i^n are decomposed as

$$\int_{\partial V_i^n} \nabla q \cdot \mathbf{n} = \sum_{f \in \text{faces}(C_i)} \int_{f \cap \Omega^n} \nabla q \cdot \mathbf{n} + \int_{\partial \Omega^n \cap C_i} \nabla q \cdot \mathbf{n}, \tag{19}$$

and since the boundary conditions (3)-(4) are homogeneous, all interfacial fluxes are null and we approximate the above as

$$\int_{\partial V_i^n} \nabla q \cdot \mathbf{n} = \sum_{f \in \text{faces}(C_i)} \nabla q \cdot \mathbf{n}\big|_f |f \cap \Omega^n| + \mathcal{O}(\Delta x^3). \tag{20}$$

The volumes $|V_i^n|$ as well as the faces fractions $|f \cap \Omega^n|$ are calculated using the second-order quadrature rules presented in [38]. The resulting linear systems are solved using a Multigrid [60] preconditioned Bi-Conjugate Gradient Stabilized solver. For the model presented in section 3, the total mass of protein at any given time t is

$$M_T(t) = M_A(t) + 2M_B(t) = \int_{\Omega(t)} \psi_A + 2\int_{\Omega(t)} \psi_B = \sum_{i=1}^{M} \int_{V_i^n} \psi_A^n + 2\sum_{i=1}^{M} \int_{V_i^n} \psi_B^n, \tag{21}$$

where $M_A(t)$ and $M_B(t)$ are the total mass of species A and B respectively. The factor 2 in front of the second integral accounts for species B being the dimer composed of two monomers, and therefore being twice as heavy. While this conservation property is easily achieved on fixed geometry, additional care is required to ensure it holds in the deforming case as we will see next.

In practice, the dynamic mesh refinement imposes to interpolate the solution between consecutive grids. To preserve the overall accuracy, we use a third-order Least Square interpolation which is unfortunately non-conservative. This interpolating step can generate local spurious converging mass variations. However, as our results illustrate, these variations are converging and, in practice, reasonably small.

Another key feature of our proposed finite volume formulation is that it does not require extending the solution across the interface as it is often required with interfacial problems (see [23,59]). Instead, our formulation only involves the solution where it is formally defined (*i.e.* inside $\Omega(t)$).

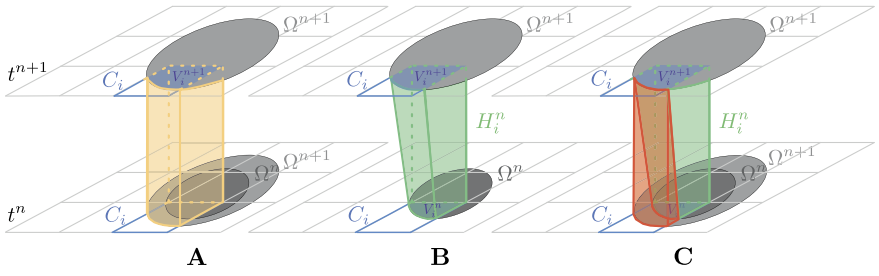

Fig. 5. Comparison between the traditional and conservative finite volume formulations: (**A**) With the traditional approach, the equation is first discretized in time and then spatially integrated over each control volume $V_i^{n+1} = C_i \cap \Omega^{n+1}$ (depicted in blue) at the future time t^{n+1}. In the spatio-temporal domain, this is an integral over the orange hyper volume. (**B**) With our proposed formulation, the partial differential equation is directly integrated over the hypervolume $H_i^n = V_i(t) \times [t^n, t^{n+1}]$, leading to mass conservation. (**C**) The local mass loss with the traditional method are directly related to the difference between the two hypervolumes (in red). (For interpretation of the colors in the figure(s), the reader is referred to the web version of this article.)

4.1.2. Traditional formulation

Here, we consider a common way of applying the finite volume method to time-dependent problem, which we will refer to as the *traditional formulation*. In this formulation we start by discretizing the conservation equations (1) and (2) in time using the semi-implicit scheme

$$\frac{\psi_A^{n+1} - \psi_A^n}{\Delta t} - D_A \triangle \psi_A^{n+1} = 2\gamma_{BA}\psi_B^n - \gamma_{AB}\left(\psi_A^n\right)^2, \tag{22}$$

$$\frac{\psi_B^{n+1} - \psi_B^n}{\Delta t} - D_B \triangle \psi_B^{n+1} = \frac{1}{2}\gamma_{AB}(\psi_A^n)^2 - \gamma_{BA}\psi_B^n, \tag{23}$$

where the upper-scripts n and $n+1$ indicate the semi-discrete quantities being evaluated at $(\mathbf{x}, t^n)$ and $(\mathbf{x}, t^{n+1})$ respectively. We construct the finite volume formulation by integrating the above Eqs. over the control volumes $V_i^n = C_i \cap \Omega^{n+1}$ (see Fig. 5). For each cell $C_{i=1,\cdots,M}$, we obtain

$$\int_{V_i^{n+1}} \psi_A^{n+1} - D_A \Delta t \int_{V_i^{n+1}} \triangle \psi_A^{n+1} = \int_{V_i^{n+1}} \left(\psi_A^n + \Delta t\left(2\gamma_{BA}\psi_B^n - \gamma_{AB}{\psi_A^n}^2\right)\right), \tag{24}$$

$$\int_{V_i^{n+1}} \psi_B^{n+1} - D_B \Delta t \int_{V_i^{n+1}} \triangle \psi_B^{n+1} = \int_{V_i^{n+1}} \left(\psi_B^n + \Delta t\left(\frac{1}{2}\gamma_{AB}{\psi_A^n}^2 - \gamma_{BA}\psi_B^n\right)\right), \tag{25}$$

which, using Gauss's theorem, we rewrite as

$$\int_{V_i^{n+1}} \psi_A^{n+1} - D_A \Delta t \int_{\partial V_i^{n+1}} \nabla \psi_A^{n+1} \cdot \mathbf{n} = \int_{V_i^{n+1}} \left(\psi_A^n + \Delta t\left(2\gamma_{BA}\psi_B^n - \gamma_{AB}{\psi_A^n}^2\right)\right), \tag{26}$$

$$\int_{V_i^{n+1}} \psi_B^{n+1} - D_B \Delta t \int_{\partial V_i^{n+1}} \nabla \psi_B^{n+1} \cdot \mathbf{n} = \int_{V_i^{n+1}} \left(\psi_B^n + \Delta t\left(\frac{1}{2}\gamma_{AB}{\psi_A^n}^2 - \gamma_{BA}\psi_B^n\right)\right). \tag{27}$$

To quantify the total mass (shown in (21)) we start by summing Eq. (26) over all grid cells,

$$\sum_{i=1}^{M}\left(\int_{V_i^{n+1}} \psi_A^{n+1} - D_A \Delta t \int_{\partial V_i^{n+1}} \nabla \psi_A^{n+1} \cdot \mathbf{n}\right) = \sum_{i=1}^{M} \int_{V_i^{n+1}} \left(\psi_A^n + \Delta t\left(2\gamma_{BA}\psi_B^n - \gamma_{AB}{\psi_A^n}^2\right)\right) \tag{28}$$

Because the diffusive fluxes are anti-symmetric and the boundary condition (3) is homogeneous, the contour integrals vanish, leaving us with

$$\sum_{i=1}^{M} \int_{V_i^{n+1}} \psi_A^{n+1} = \sum_{i=1}^{M} \int_{V_i^{n+1}} \left(\psi_A^n + \Delta t\left(2\gamma_{BA}\psi_B^n - \gamma_{AB}{\psi_A^n}^2\right)\right), \tag{29}$$

which in terms of the total mass M_A of the monomer A reads

$$M_A^{n+1} = \sum_{i=1}^{M} \int_{V_i^{n+1}} \psi_A^n + \Delta t \sum_{i=1}^{M} \int_{V_i^{n+1}} \left(2\gamma_{BA}\psi_B^n - \gamma_{AB}{\psi_A^n}^2\right). \tag{30}$$

Similarly we obtain for the second specie

$$M_B^{n+1} = \sum_{i=1}^{M} \int_{V_i^{n+1}} \psi_B^n + \Delta t \sum_{i=1}^{M} \int_{V_i^{n+1}} \left(\frac{1}{2}\gamma_{AB}\psi_A^n - \gamma_{BA}{\psi_B^n}^2\right). \tag{31}$$

Multiplying Eq. (31) by two and adding the result to Eq. (30), the reactive terms cancel and it results

$$M_T^{n+1} = M_A^{n+1} + 2M_B^{n+1} = \sum_{i=1}^{M} \int_{V_i^{n+1}} \left(\psi_A^n + 2\psi_B^n\right). \tag{32}$$

Because the volumes over which the integrals are performed are evaluated at time step t^{n+1} while the integrands are evaluated at t^n, the right-hand side is not the total mass at t^n and therefore, with this semi-discrete formulation, $M_T^{n+1} \neq M_T^n$. Another issue resulting from this asynchronicity is that the quantities ψ_A^n, ψ_B^n may not be formally defined over the control volumes V_i^{n+1}, and therefore they may have to be extended over the interface $\partial\Omega^n$ before being integrated in Eqs (26) and (27). Such extensions are often expensive as they involve costly geometric reconstruction [54,23] or solving non-linear propagation equations [6,58], and may not preserve the stability of the method.

4.1.3. Conservative formulation

Inspired by the work of Gaburro et al. [22], we construct the conservative formulation by integrating Eqs. (1) and (2) over the space-time hyper volume $H_i^n = V_i(t) \times [t^n, t^{n+1}]$ (see Fig. 5). Focusing on the monomer A we obtain

$$\int_{H_i^n} \left(\frac{\partial \psi_A}{\partial t} - D_A \triangle \psi_A\right) = \int_{H_i^n} \left(2\gamma_{BA}\psi_B^n - \gamma_{AB}\left(\psi_A^n\right)^2\right), \tag{33}$$

which in virtue of Gauss's theorem can be rewritten as

$$\int_{V_i^{n+1}} \psi_A^{n+1} - \int_{V_i^n} \psi_A^n - D_A \int_{t^n}^{t^{n+1}} \int_{\partial V_i(t)} \nabla\psi_A \cdot \mathbf{n} = \int_{H_i^n} \left(2\gamma_{BA}\psi_B - \gamma_{AB}\left(\psi_A\right)^2\right). \tag{34}$$

Integrating the diffusive terms implicitly and the reactive ones explicitly, the semi-discrete formulation becomes

$$\int_{V_i^{n+1}} \psi_A^{n+1} - \int_{V_i^n} \psi_A^n - D_A \Delta t \int_{\partial V_i(t)} \nabla\psi_A \cdot \mathbf{n} = \Delta t \int_{V_i^n} \left(2\gamma_{BA}\psi_B - \gamma_{AB}\left(\psi_A\right)^2\right), \tag{35}$$

and similarly

$$\int_{V_i^{n+1}} \psi_B^{n+1} - \int_{V_i^n} \psi_B^n - D_B \Delta t \int_{\partial V_i(t)} \nabla\psi_B \cdot \mathbf{n} = \Delta t \int_{V_i^n} \left(\frac{1}{2}\gamma_{AB}\psi_A^n - \gamma_{BA}{\psi_B^n}^2\right). \tag{36}$$

To prove that this formulation is conservative, we again sum the formulation over all computational cells, use the anti-symmetry of the fluxes and the homogeneity of the boundary condition (3) to conclude that

$$M_A^{n+1} = \sum_{i=1}^{M} \int_{V_i^n} \psi_A^n + \Delta t \sum_{i=1}^{M} \int_{V_i^n} \left(2\gamma_{BA}\psi_B^n - \gamma_{AB}{\psi_A^n}^2\right). \tag{37}$$

The only difference between the above equation and (30) is that the first integral in the right-hand side is now evaluated on the geometry at t^n. It implies that the sum is indeed the total mass of A at t^n

$$M_A^{n+1} = M_A^n + \Delta t \sum_{i=1}^{M} \int_{V_i^n} \left(2\gamma_{BA}\psi_B^n - \gamma_{AB}{\psi_A^n}^2\right), \tag{38}$$

and similarly

$$M_B^{n+1} = M_B^n + \Delta t \sum_{i=1}^{M} \int_{V_i^{n+1}} \left(\frac{1}{2} \gamma_{AB} \psi_A^n - \gamma_{BA} {\psi_B^n}^2 \right), \tag{39}$$

leading to the total conservation

$$M_A^{n+1} + 2M_B^{n+1} = M_A^n + 2M_B^n \quad \Longleftrightarrow \quad M_T^{n+1} = M_T^n. \tag{40}$$

We conclude that this formulation is mass-conservative.

4.1.4. Convergence limitations of the traditional formulation

As we exposed, the traditional finite volume method fails to preserve mass. We find here an upper bound for its accuracy. From this result, we demonstrate that the total mass loss, and by extension the concentration, is not guaranteed to converge. We conduct this analysis on a uniform grid for readability and denotes by Δx the spatial resolution.

To quantify the total mass variation Δ_M^n between two consecutive time steps

$$\Delta_M^n = M_T^{n+1} - M_T^n = \sum_{i=1}^{M} \left(\int_{V_i^{n+1}} \psi_A^n + 2\psi_B^n - \int_{V_i^n} \psi_A^n + 2\psi_B^n \right), \tag{41}$$

we start by reformulating Eq. (32) as

$$M_T^{n+1} - \sum_{i=1}^{M} \int_{V_i^{n+1}} \left(\psi_A^n + 2\psi_B^n \right) = 0, \tag{42}$$

and decomposing each integrals over the domains V_i^n and $V_i^{n+1} \setminus {V_i}^n = \Lambda_i^n$ (visualized in Fig. 5-(C) as the red shaded region).

$$M_T^{n+1} - \sum_{i=1}^{M} \int_{V_i^n} \left(\psi_A^n + 2\psi_B^n \right) = \sum_{i=1}^{M} \int_{\Lambda_i^n} \left(\psi_A^n + 2\psi_B^n \right). \tag{43}$$

The left-hand side term is exactly Δ_M^n, and so after taking the absolute value we obtain

$$|\Delta_M^n| \leq \sum_{i=1}^{M} \int_{\Lambda_i^n} |\psi_A^n + 2\psi_B^n|, \tag{44}$$

Because only for the computational cells that are crossed by the interface during the interval $[t^n, t^{n+1}]$ the integral over Λ_i^n is non-zero, we can further simplify the above inequality and write that

$$|\Delta_M^n| \leq M_\Gamma^n \quad \max_i |\Lambda_i^n| \quad ||\psi_A^n + 2\psi_B^n||_\infty, \tag{45}$$

where M_Γ^n is the total number of cells crossed by the interface during $[t^n, t^{n+1}]$. Provided that the time step is small enough, this total number scales as $\frac{1}{\Delta x^{d-1}}$, d being the spatial dimension. The size of the volume variation $|\Lambda_i^n|$ is order of the local interface displacement multiplied by the area of the surface contained in V_i^n, therefore $|\Lambda_i^{n+1}| = \mathcal{O}(\Delta x^{d-1} \Delta t)$. Assuming that the concentration field remains bounded, we obtain the following approximation for the local mass loss

$$\Delta_M^n = \mathcal{O}(\Delta t), \tag{46}$$

telling us that the global mass loss is $\mathcal{O}(1)$. This proves that the mass loss are non-diverging, but we cannot conclude whether they are converging or not. However, we can construct a simple example[1] where the upper bound in Eq. (44) is reached, proving that in general the total mass is not converging and therefore that concentration is also not converging in L^∞-norm.

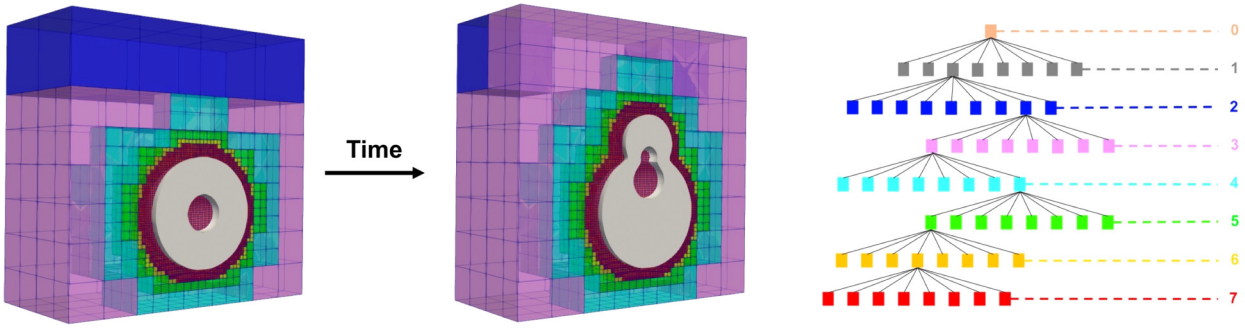

Fig. 6. Adaptive grid generation and representation. The level of a computational cell is defined as the number of successive subdivisions to create it. In this example the maximum level is 7 (red cells) and the minimum level is 2 (blue cells). The automatic refinement is done according to criterion (47)-(48).

4.2. Adaptive mesh refinement

The computational domain is represented as a non-graded octree grid [8]. At each iteration, the mesh generation starts with the root cell representing the entire domain (corresponding to level the 0) and, which we subdivide into eight identical cells of level 1 (see Fig. 6). We then recursively divide each newly created cell C if either

$$\min_{v\in \text{nodes}(C)} |\phi(v)| \leq \text{Lip}(\phi)\cdot D(C) \quad \text{and} \quad \text{level}(C) < \max_{\text{level}}, \tag{47}$$

or

$$\text{level}(C) < \min_{\text{level}}, \tag{48}$$

where $\text{Lip}(\phi)$ is an estimation of the minimal Lipschitz constant for the level set function $\phi(\mathbf{x})$, set to 1.2 in practice, $D(C)$ is the length of the diagonal C, $\min_{\text{level}}$ and $\max_{\text{level}}$ are the prescribed minimum and maximum tree level. As it was done in our previous study [61], we store the concentrations at the cell centers and the level set values at the nodes. Because the interface is evolving between iterations, the grid is too and the solution must be interpolated between grids. This is achieved using third-order Least Square regression as it was done in our previous studies [23,61,59].

5. Numerical validations

In this section, we compare our conservative formulation to the traditional one, in both two and three spatial dimensions. We first consider a simpler test problem for which we construct an analytic solution allowing us to investigate the convergence of the solution. We then return to our motivating application and focus on total mass conservation. In both cases, we find that our method converges with second-order accuracy in space while the traditional approach rapidly stalls.

5.1. Test problem: expanding sphere

To study the spatio-temporal convergence of the two formulations, we consider a one-species diffusion system with an exact solution on an expanding and translating sphere. We define this spherical domain by the level set function

$$\phi_{exact}(t) = |\mathbf{x} - \mathbf{x}_0(t)| - r(t), \tag{49}$$

where $r(t) = 0.25t$ is the expanding radius and $\mathbf{x}_0(t) = (0, t, 0)$ is the translating center. In this domain we consider the following test problem for a single concentration field $\psi(\mathbf{x}, t)$

$$\frac{\partial \psi}{\partial t} - \triangle \psi = f(\mathbf{x}, t), \qquad \forall \mathbf{x} \in \Omega(t), \tag{50}$$

$$\nabla \psi \cdot \mathbf{n} = g(\mathbf{x}, t), \qquad \forall \mathbf{x} \in \partial\Omega(t). \tag{51}$$

We use for the exact solution $\psi_{exact}(\mathbf{x}, t)$, forcing term $f(\mathbf{x}, t)$ and boundary flux $g(\mathbf{x}, t)$ the functions

$$\textbf{2D} \quad \psi_{Exact}(\mathbf{x}, t) = e^{x+y+t}, \quad f(\mathbf{x}, t) = -e^{x+y+t}, \quad g(\mathbf{x}, t) = e^{x+y+t}, \tag{52}$$

$$\textbf{3D} \quad \psi_{Exact}(\mathbf{x}, t) = e^{x+y+z+t}, \quad f(\mathbf{x}, t) = -2e^{x+y+z+t}, \quad g(\mathbf{x}, t) = e^{x+y+z+t}, \tag{53}$$

[1] Consider, for example, a flat interface moving at a constant speed V, with uniform concentration and fields, and a fixed time step $\Delta_t = \frac{\Delta x}{V}$. In this example, there are exactly $\frac{1}{\Delta x}$ many Λ_i^{n+1}, which are all identical and of size Δx^2, and thus the upper bound in Eq. (44) is reached.

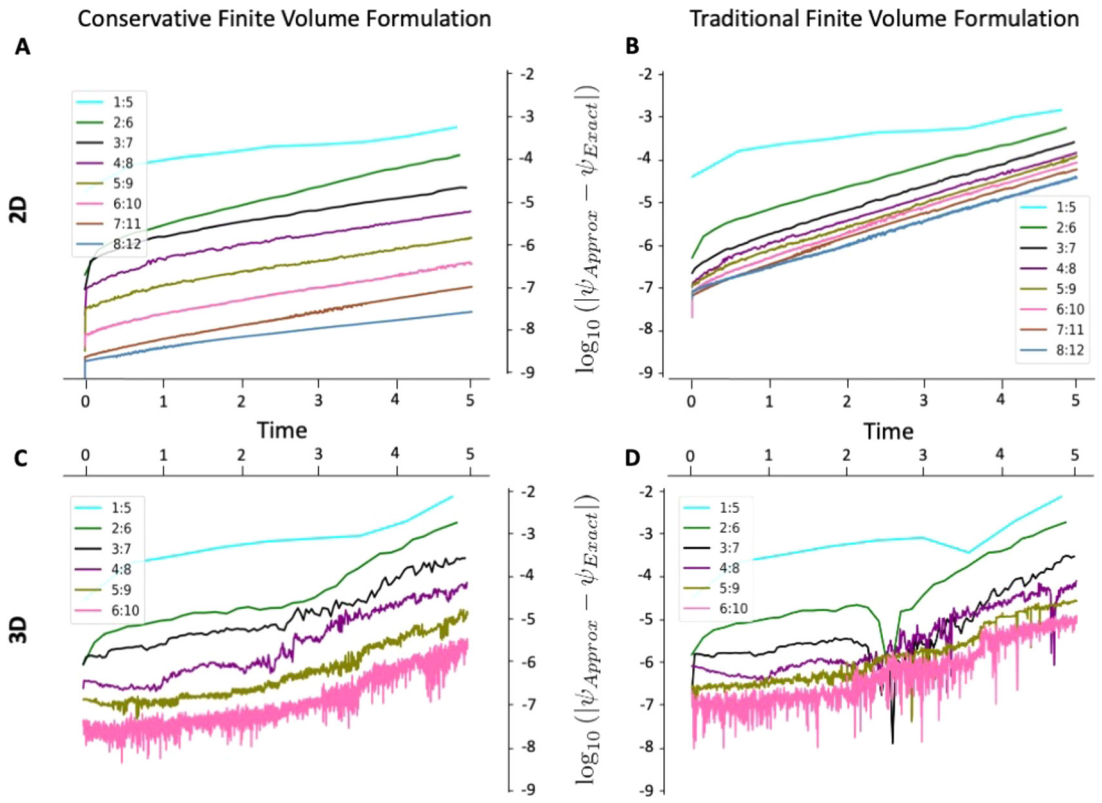

Fig. 7. Expanding sphere - Convergence of our conservative (left column) and the traditional (right Column) formulations for the expanding sphere test 5.1, in two (**A-B**), and three spatial dimensions (**C-D**).

Table 1
Convergence of the global $L^\infty-$error with the proposed and traditional formulations, in two and three spatial dimensions. Results are indexed by the minimum and maximum grid levels.

	2D			
	Conservative FV		Traditional FV	
levels	error	order	error	order
1:5	9.76×10^{-4}	-	1.12×10^{-3}	-
2:6	2.15×10^{-4}	2.18	4.36×10^{-4}	1.37
3:7	3.74×10^{-5}	2.52	2.03×10^{-4}	1.09
4:8	1.02×10^{-5}	1.87	1.14×10^{-4}	0.83
5:9	2.46×10^{-6}	2.06	9.74×10^{-5}	0.23
6:10	6.52×10^{-7}	1.92	6.86×10^{-5}	0.51
7:11	1.71×10^{-7}	1.93	4.78×10^{-5}	0.52
8:12	4.41×10^{-8}	1.96	3.21×10^{-5}	0.57

	3D			
	Conservative FV		Traditional FV	
levels	error	order	error	order
1:5	6.83×10^{-3}	-	6.83×10^{-3}	-
2:6	1.69×10^{-3}	2.01	1.69×10^{-3}	2.01
3:7	2.56×10^{-4}	1.96	2.72×10^{-4}	2.64
4:8	6.86×10^{-5}	2.07	6.85×10^{-5}	1.99
5:9	1.64×10^{-5}	2.06	2.43×10^{-5}	1.50
6:10	4.24×10^{-6}	1.95	1.07×10^{-5}	1.18

and run the simulation for $t \in [0, 5]$. Because we expect our new formulation to be first-order in time and second-order in space - *i.e.* $\mathcal{O}(\Delta t + \Delta x^2)$ -, we let $\Delta t = 1000\Delta x^2$, so that the measured numerical error is $\mathcal{O}(\Delta x^2)$. To decrease the resolution, we increase both the minimum and maximum levels of the grid. Doing so, we ensure that the spatial resolution diminishes everywhere. Increasing only the maximum level would only refine the grid close to the interface.

Fig. 7 depicts the time evolution of the L^∞-error for increasing grid resolutions. In two dimensions, our method is converging at an apparent constant rate, while the traditional finite volume formulation appears to stall after two refinements ($\max_{\text{level}} = 7$). It results in a solution orders of magnitude more accurate with our conservative formulation. The same observations apply to the three-dimensional results, even though the differences between the two methods are less striking as the analysis is limited to a $\max_{level} = 10$.

The corresponding orders of convergence for the global L^∞-errors are reported in Table 1. The conservative formulation is second-order accurate in space and at least first order in time in two and three dimensions. With the non-conservative method, the order of convergence decreases as the resolution increases. This accuracy drop is flagrant in two dimensions, where the order rapidly falls around 0.5. In comparison, the three-dimensional order only drops to 1.18.

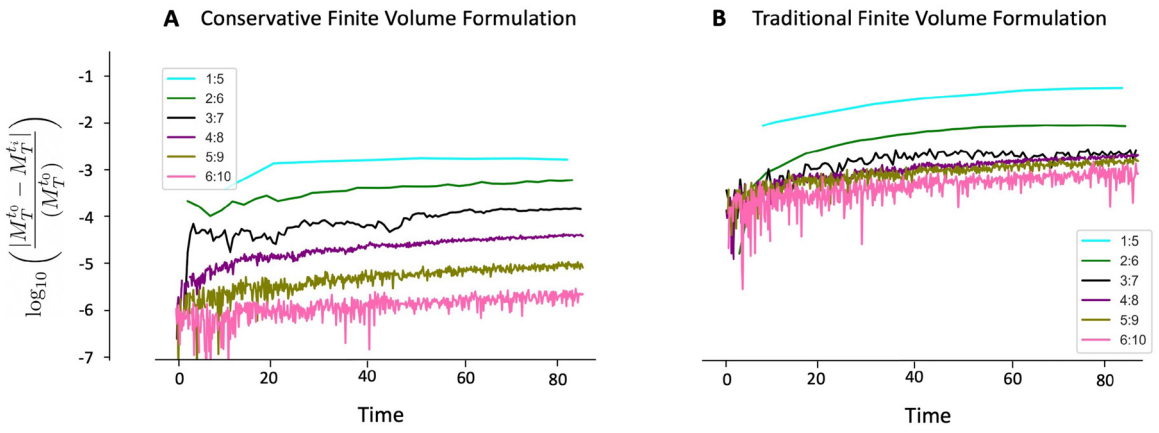

Fig. 8. Semi-log plot of relative mass loss for the conservative (**A**) and traditional FV (**B**). Again the curves are labelled by their minimum and maximum grid level. We observe that the traditional method rapidly stalls while the conservative one provide converging mass loss over the considered range of grid resolution.

Table 2
Mass loss for the biological application, using either our methods. Results are indexed by the minimum and maximum grid levels.

	3D			
	Conservative FV		Traditional FV	
Levels	mass loss	order	mass loss	order
1:5	2.56×10^{-3}	-	6.06×10^{-2}	-
2:6	8.74×10^{-4}	1.55	9.66×10^{-3}	2.65
3:7	2.13×10^{-4}	2.03	3.02×10^{-3}	1.68
4:8	5.68×10^{-5}	1.91	2.31×10^{-3}	0.38
5:9	1.46×10^{-5}	1.95	1.98×10^{-3}	0.22
6:10	3.86×10^{-6}	1.92	1.64×10^{-3}	0.28

5.2. Practical mass conservation

To quantify the mass conservation of both methods, we go back to the original biological motivation described by the system (1)-(2), and consider the three-dimensional Splitting Nucleus geometry with the geometric parameters listed in 3. Simulations are carried until the final time $T = 90$ min at which point the daughter cell has fully detached from the mother cell. We set the diffusion coefficients to be $D_A = 10^3$ μm$^2 \cdot$ min^{-1} and $D_B = 1$ μm$^2 \cdot$ min^{-1}. The reaction rates are $\gamma_{AB} = 10^{-2}$ μm$^3 \cdot$ min^{-1} and $\gamma_{BA} = 10^{-3}$ min^{-1}. We define the relative total mass variations at any given discrete time t^n in terms of the initial and current total mass

$$e_M(t^n) = \left| \frac{M_T^n - M_T^0}{M_T^0} \right|, \tag{54}$$

where the current total mass is calculated as

$$M_T^n = \int_{\Omega^n} \psi_A^{n+1} + 2\psi_B^{n+1}. \tag{55}$$

The mass loss as a function of time and for increasing grid resolution, using either method is depicted in Fig. 8, and the estimated orders of convergence are reported in Table 2. As for the previous error analysis, our formulation converges at an apparent second-order rate, while the traditional method stalls after a couple of refinement. Again the error differences between the two methods are striking: they reach three orders of magnitudes on the finest grid ($\max_{\text{level}} = 10$). The mass loss with our method on the coarsest grid is comparable to the one obtained with the traditional on the finest grid.

For the rest of our biological study, we will set the minimum and maximum grid levels to 5 and 8, respectively. In light of the measurement reported in Fig. 8 we are confident that the typical mass loss will be well below 0.1%.

Table 3
Simulation parameters for the dividing yeast cell (section 6.1).

	Parameter	Symbol	Value	References
Geometry	Budding time	T	90 min	[11]
	Mother radius	r_m	2.07 µm	[63]
	Daughter final radius	r_d	1.81 µm	[63]
	Nucleus radius	r_n	0.89 µm	[37,66]
	Estimated IPOD and JUNQ length	-	0.28 µm	[30,45]
Biochemistry	Characteristic concentration	ψ_0	713 μm^{-3}	[19]
	Typical diffusivity	-	24-120 $\mu m^2 min^{-1}$	[37]
	Typical fragmentation rate	γ_{BA}	1.35×10^{-3} min^{-1}	[65]
	Typical aggregation rate	γ_{AB}	2.57×10^{-4} $\mu m^3 \cdot$ min^{-1}	[65]
Computational	Domain length	-	7.5 µm	
	Grid levels	-	5:8	
	Grid resolution	-	29 nm - 234 nm	
	Time step	Δt	12 s	

6. Simulated prions dynamics in dividing yeast cells

6.1. Simulation parameters

We provide all parameter values in Table 3 and summarize here how they were obtained. Bryne et al. [11] found the cell reproduction time to be 1.46 hours on average (for the strains YJW512 [PSI +]); based on this we took the cell division time (*i.e.* the final time) to be $T = 90$ min. Next, we chose 37 μm^3 as the volume of the mother cell at the initial time according to Tyson et al. [63]; from the same reference, we have that the volume of the daughter cell must be two-thirds of the volume of the mother cell when budding is complete. For the nucleus size, we use the estimation provided in [37], which is in reasonable agreement with the experimental observations of Wang et al. [66]. We model the additional compartments in the mother cell to resemble the IPOD and JUNQ compartments found in yeast cells, which are known to affect protein aggregation. Although the size and shape of these compartments are known to vary, we chose to represent these compartments as ellipsoids for simplicity. We selected their characteristic lengths to be smaller than the nucleus, based on microscopic observations found in [45].

We estimate the characteristic prion concentration ψ_0 from the value reported on the Saccharomyces Genome Database [19]. For the typical rates of fragmentation and aggregation, γ_{BA} and γ_{AB} respectively, we chose values in agreement with our previous study [65]. We note that these findings were obtained in a different context, and so the typical rates (reported in Table 3) will only be used as guiding information during our computational exploration. In all of our simulations, we use constant initial concentration fields with random spatial noise. These initial profiles are re-scaled so that the initial total mass is identical across all examples. For the rest of this manuscript, we will use the minute and micrometer as our characteristic time and length scales and non-dimensionalize all concentrations by the characteristic concentration ψ_0. From now on, all quantities will be reported in dimensionless form.

In this last section, we return to the original biological motivation, the simulation of prion dynamics in dividing yeast cells, and characterize the impact of the biochemical properties and geometric features on the proteins distributions. We conduct this analysis in two steps, focusing first on a purely diffusive system and exposing the limitations of the well-mixed assumption as the system representation complexifies. We then turn our attention to the full reaction-diffusion system and quantify the asymmetries in the species repartition.

6.2. Diffusive system - limitations of the well-mixed assumption

To quantify the impact of the diffusion alone we first simulate a purely diffusive system (*i.e.* $\gamma_{AB} = \gamma_{BA} = 0$). Because the two protein species are now decoupled, we will focus on species A only and assume that $\psi_B = 0$. For each geometrical representation, we vary the diffusion rate from 10^{-7} to 10^5, scanning in particular through the biologically relevant range ($\approx 10^1 - 10^2$, shown in Table 3), and measure the amount of transmitted material in two ways. First, we compute $F_A(t)$ the fraction of total mass transferred to the daughter cell

$$F_A(t) = \frac{\int_{\Omega_D(t)} \psi_A}{\int_{\Omega_D(t)\cup\Omega_M(t)} \psi_A} = \frac{\int_{\Omega_D(t)} \psi_A}{M_T^0} \tag{56}$$

where $\Omega_M(t)$ ad $\Omega_D(t)$ denote the inside of the mother and daughter cells at time t, and M_T^0 is the initial total mass. Second, we compute F_C, the final ratio of average concentrations between the mother and daughter cells

$$F_C = \frac{\int_{\Omega_D(T)} \psi_A}{\int_{\Omega_M(T)} \psi_A} \frac{|\Omega_M(T)|}{|\Omega_D(T)|}, \tag{57}$$

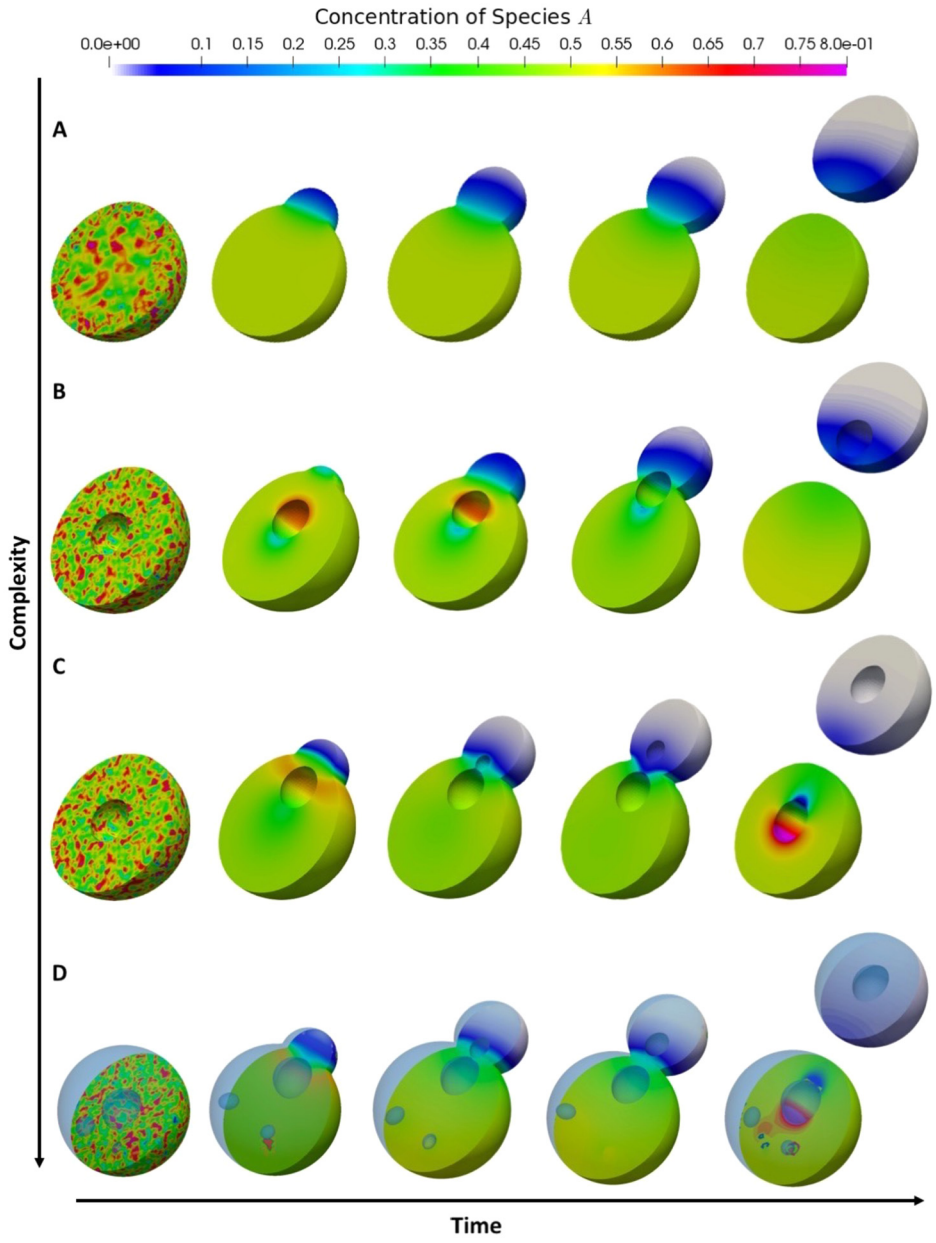

Fig. 9. Prions diffusion in dividing yeast cells for geometries of increasing complexity and $D_A = 10^{-3}$. The concentration profile is represented in characteristic concentration units ($\psi_0 = 713\ \mu m^{-3}$). **A** No nucleus, **B** Moving nucleus, **C** Splitting nucleus, and **D** Splitting nucleus with additional moving compartments.

For a symmetric transfer from the mother to the daughter cell, we expect the average concentration in both final cells to be identical, and so the concentration ratio F_C to be 1, and the final mass ratio $F_M(T)$ to only depend on the cells volume and be $\frac{|\Omega_D(T)|}{|\Omega_D(T)|+|\Omega_M(T)|}$, which for the chosen radii (see Table 3), and in the absence of nuclei or compartments, is 0.4.

The diffusion process for all four geometries is depicted in Fig. 9. The fraction of final mass for all geometries and all considered diffusion coefficients is represented in Fig. 10. Unsurprisingly the fraction of mass remains under 0.4 (the ideal value for a perfectly symmetric transfer) even for the fastest diffusion and the least obstructed geometry (for case **A**, $D_A = 10^3$, we measure $F_M(T) = 0.38$). The final separation between the two cells happens around $t = 80$. After this time, the daughter mass cannot change, despite the daughter cell still moving and growing. Indeed, we observe the daughter's mass to be constant after this point in all cases. We interpret this as another illustration of the conservation property of our finite volume formulation.

The addition of the nucleus seems to have the most dramatic impact on the transfer process, as it reduces the daughter's mass by around 50%. Furthermore, including the split of the nucleus or additional cellular compartments reduces each time

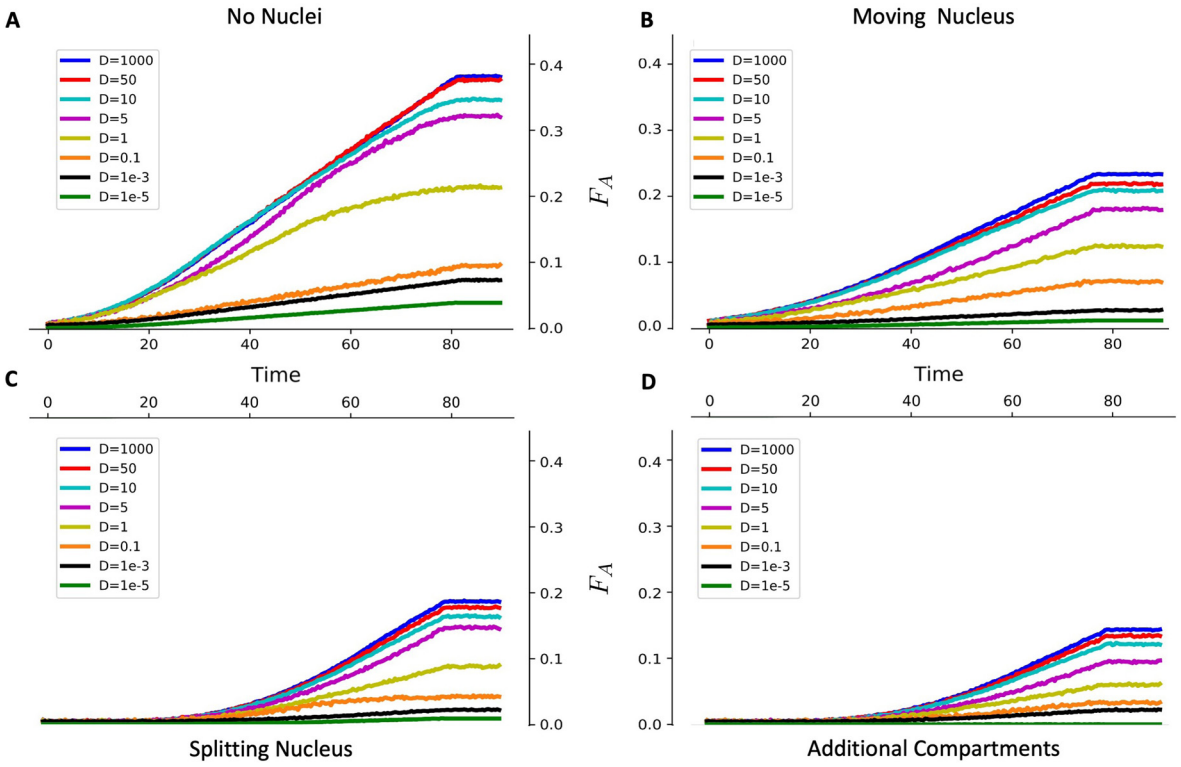

Fig. 10. Fraction of total mass in the daughter cell as a function of time for various diffusion rates. In **A**, where there is no nucleus, about 40% of the mass is transferred to the daughter cell for fast diffusion rates. The addition of obstacles drastically reduces the amount of transmitter material. **B** Moving Nucleus. **C** Splitting Nucleus. **D** Additional compartments in the cell.

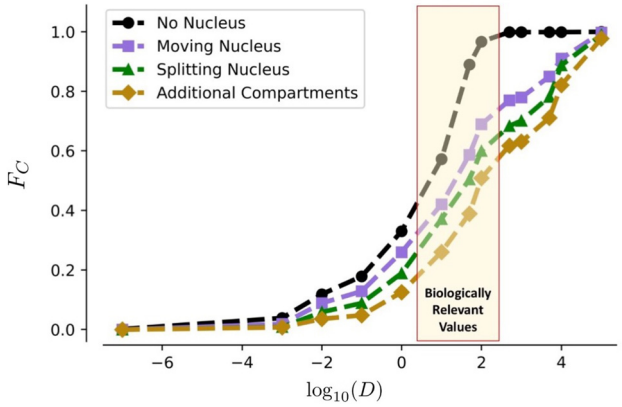

Fig. 11. Ratio of the final average concentration in the daughter and mother cells (F_C) for varying diffusion coefficient (D). As expected, almost no mass is transferred between the mother and daughter cells for very slow diffusion rates. At the other extreme, the system is well-mixed, and the concentrations are identical (ratio of 1). For biologically relevant diffusion rates, we find that the system is far from an ideal well-mixed environment. The system's complexity amplifies this discrepancy.

the transmission by another 10% to 15%. Ultimately, for the most realistic representations (B, C, D), the transmission is largely asymmetric, suggesting that the diffusive process alone can generate asymmetries and that the well-mixed assumption is irrelevant.

To further investigate these asymmetries and the validity of the well-mixed assumption, we turn our attention to Fig. 11 where the final concentration ratios are reported. Again, an ideal well-mixed system would lead to an ideal transfer and a ratio of 1. A ratio of 0 indicates that no transfer occurred. For the most realistic geometries (B, C, D), the ideal transmission limit is only approached for the largest diffusion coefficients, which are likely order of magnitude larger than the biological ones. The well-mixed assumption for such a system is therefore largely inaccurate. Most interestingly, the transition from a non-transferring system ($F_C = 0$) to an ideal well-mixed system ($F_C = 1$) appears to be centered around the biologically

relevant diffusion values. This observation suggests that the biological system may lie where the diffusion coefficient variations have their largest impact. In other words, this hints that the biological system may be hypersensitive to the prions diffusivity.

6.3. Full system - asymmetric distributions

For this final study, we consider the full systems and quantify the impacts of the reaction rates on the asymmetry of the transfer for each protein species. We set the diffusion coefficients ($D_A = 10^3$, $D_B = 1$) so that they are close to the biologically relevant range. We chose D_B to be less than D_A because species B is bigger, and therefore expected to be less mobile. We will consider the splitting nucleus geometry only and quantify the transfer process by computing the final mass fraction of each specie

$$F_A(T) = \frac{\int_{\Omega_D(T)} \psi_A}{M_T^0} \qquad \text{and} \qquad F_B(T) = \frac{2\int_{\Omega_D(T)} \psi_B}{M_T^0}. \tag{58}$$

For a single species, the final mass fraction in the daughter cell does not exceed 0.2 (see Fig. 10 **C**). Because all our initial conditions are re-scaled to have the same total mass, the final mass fraction of either species cannot exceed 0.2. If either one of them reaches this value, it indicates that the other species has been depleted. In the current context, we will define a perfectly symmetric transfer as one where the above final ratios are identical.

The reaction-diffusion process is illustrated on Fig. 12. Both concentrations appear to be quasi-uniform in each cell and sharply varying over the bud neck. These localized spatial heterogeneities seem to be the main explanations for the large concentration asymmetries we observed at the final stage. This suggests that the area of the bud neck over which the cellular material is transferred is crucial in the transmission process.

In the same Figure, we display the final fraction of each species for varying reaction rates. As expected, when one of the reaction rates becomes extremely large (top left and bottom right corners of the diagrams), one of the species will be almost depleted while the mass ratio of the other one will approach the maximum ratio (0.2). Furthermore, in the vicinity of the biologically relevant rates, we observe that the fraction of species A is about two times larger than this of species B, indicating a clear asymmetry in the transmission process. We expect this unbalanced transfer will occur each time a new cell is created, and therefore that the ratio asymmetries between the youngest cells and the oldest will magnify with the generational gap's length. We note that these observations are consistent with previous experimental and computational studies of the yeast $[PSI^+]$ prion system [21].

7. Discussion & conclusions

Motivated to understand asymmetric transfers in dividing yeast cells, we proposed a novel numerical framework for reaction-diffusion systems in a three-dimensional deforming domains. Using finite volume discretizations, level set functions, and adaptive octree grids, our framework can produce accurate simulations at an enhanced computational cost while offering extreme modeling flexibility. The cornerstone of our approach is our novel finite volume formulation, where the partial differential equations are integrated over spatio-temporal control volumes. As we demonstrated, this procedure ensures mass conservation and produces a converging solution, which a traditional finite volume discretization may not achieve.

Using this new computational tool, we demonstrated how spatial heterogeneity can cause asymmetric protein transfer in dividing yeast cells and studied the effect of the yeast geometry, the mobility of the prions, and the reaction rates. We found that diffusion alone can create asymmetries, and even more so for realistic parameters and geometries. This leads us to conclude that the well-mixed assumption is not pertinent for such systems. Looking at the full reaction-diffusion model, we were able to quantify the transfer of each protein species from the mother to the daughter cell for a wide range of reaction rates. We found that our system produces large asymmetries reminiscent of these observed in experimental setups for plausible estimations of these rates.

Our reaction-diffusion model is probably too simple to produce a comprehensive simulation of the entire transmission process, yet it succeeds at reproducing experimentally observed features and provide valuable insights for future modeling strategy. Our exploration revealed sharp spatial variations across the bud neck, intuiting that the geometry of neck may be crucial for the transmission process. This suggests that either the model or the computational grid may need to be refined in that area, or that perhaps a reduced two-dimensional model of the bud neck can capture the essence of this problem.

The flexibility of our framework makes it a method of choice for studying complex intracellular biophysical processes and virtually any reaction-diffusion system on a deforming domain. The reaction-diffusion system can easily be modified to include more protein species, different initial populations, production and destruction rates, or other biological processes while preserving mass conservation. In addition, the cell shape can be refined to better match experimental observations, and other cellular entities can be integrated to better reflect how complex of an environment a cell is.

As microscopic imaging technologies advance, high-fidelity modeling strategies for studying sub-cellular protein dynamics aggregation models and simulations are required to match and support experimental data. This work lays the foundation of a new class of continuum modeling techniques for efficient and accurate simulation of intracellular processes, which we believe can help the scientific community shine the light on some essential biophysical mechanisms, a necessary first step to understand diseases and develop new treatments.

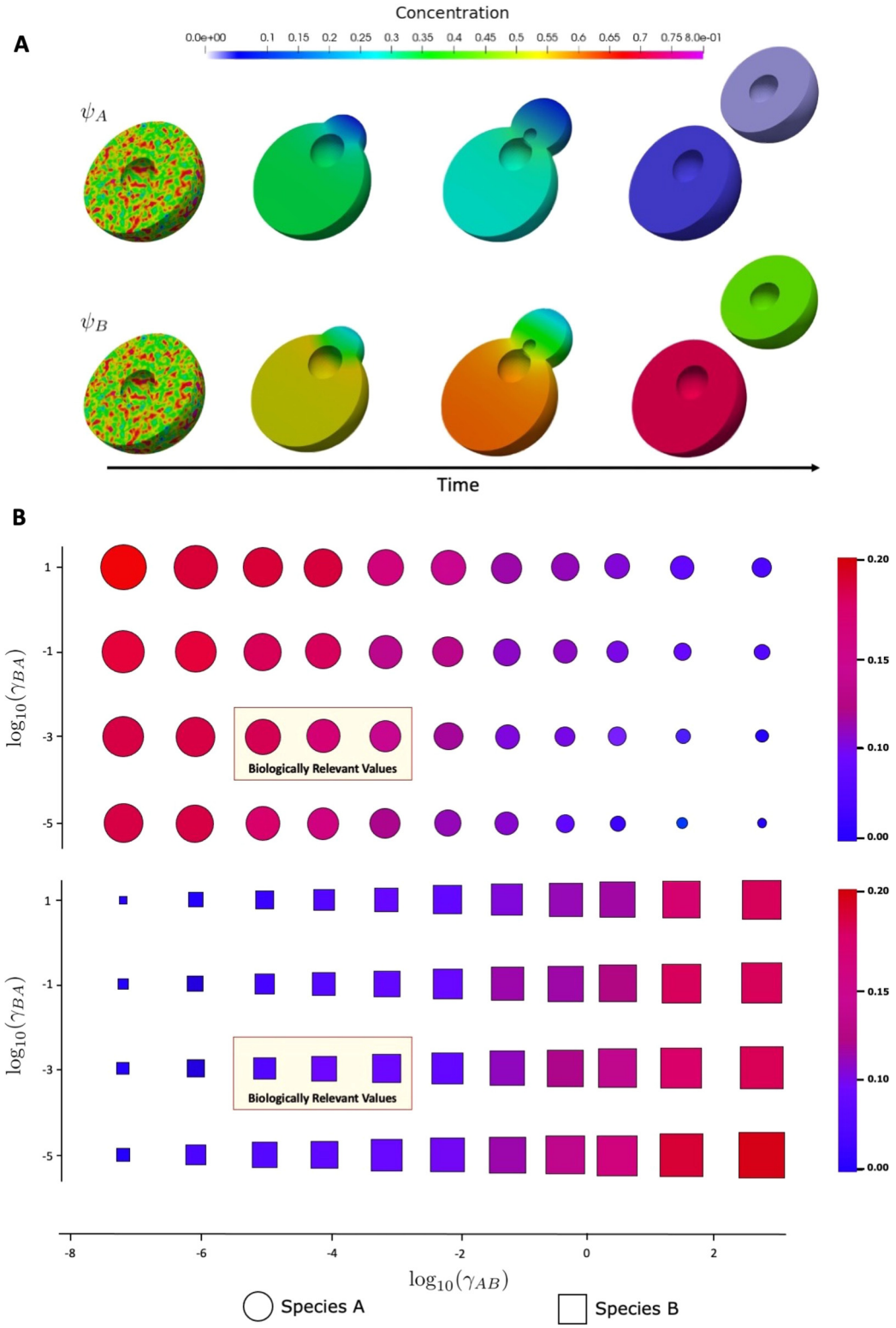

Fig. 12. Asymmetric mass transfer in dividing yeast cell - **A** Concentration profiles for $\gamma_{BA} = 10^{-3}$, $\gamma_{AB} = 1$, $D_A = 10^3$ and $D_B = 1$. **B** Final mass fractions in the daughter cell $(F_A(T),\ F_B(T))$.

CRediT authorship contribution statement

A. Ali Heydari: Formal analysis, Investigation, Software, Validation, Visualization, Writing – original draft, Writing – review & editing. **Suzanne S. Sindi:** Conceptualization, Funding acquisition, Project administration, Supervision, Writing – original draft, Writing – review & editing. **Maxime Theillard:** Conceptualization, Formal analysis, Methodology, Project administration, Software, Supervision, Writing – original draft, Writing – review & editing.

Declaration of competing interest

The authors declare that they have no known competing financial interests or personal relationships that could have appeared to influence the work reported in this paper.

Computational environment

Our solver was implemented in C++ 17, and all computations were done in parallel on CPUs using OpenMP [18,46] libraries. Three-dimensional visualizations were generated using ParaView [2] (version 5.5.2).

Acknowledgements

This research was sponsored in part by the Joint DMS/NIGMS Initiative to Support research at the Interface of the Biological and Mathematical Sciences (R01-GM126548) and National Science Foundation (DMS-1840265). The authors acknowledge support through the Data-Intensive Research and Computing program at the University of California, funded by the National Science Foundation (DMS-1840265) and computing time on the Multi-Environment Computer for Exploration and Discovery (MERCED) cluster at the University of California, Merced, which was funded by National Science Foundation Grant No. ACI-1429783. The authors would like to thank Thomas Bellotti for fruitful discussions during the early stages of the project and Anna Kucherova for feedback and comments on the manuscript before submission.

References

[1] J.U. Adams, Essentials of Cell Biology, NPG Education, Cambridge, MA, 2010.
[2] J.P. Ahrens, B. Geveci, C.C.W. Law, Paraview: an end-user tool for large-data visualization, in: The Visualization Handbook, 2005.
[3] J. Albert, A hybrid of the chemical master equation and the gillespie algorithm for efficient stochastic simulations of sub-networks, PLoS ONE 11 (3) (2016) e0149909.
[4] M.A. Alias, P.R. Buenzli, A level-set method for the evolution of cells and tissue during curvature-controlled growth, Int. J. Numer. Methods Biomed. Eng. 36 (1) (2020) e3279.
[5] A. Amoussouvi, L. Teufel, M. Reis, M. Seeger, J.K. Schlichting, G. Schreiber, A. Herrmann, E. Klipp, Transcriptional timing and noise of yeast cell cycle regulators—a single cell and single molecule approach, NPJ Syst. Biol. Appl. 4 (1) (2018) 17.
[6] T.D. Aslam, A partial differential equation approach to multidimensional extrapolation, J. Comput. Phys. 193 (1) (2004) 349–355.
[7] A.S. Association, Fatal familial insomnia, 2019.
[8] I. Babushka, J. Chandra, J.E. Flaherty, Adaptive Computational Methods for Partial Differential Equations, vol. 16, SIAM, 1983.
[9] T. Bellotti, M. Theillard, A coupled level-set and reference map method for interface representation with applications to two-phase flows simulation, J. Comput. Phys. 392 (2019) 266–290.
[10] D. Botstein, S.A. Chervitz, M. Cherry, Yeast as a model organism, Science 277 (5330) (1997) 1259–1260.
[11] L.J. Byrne, D.J. Cole, B.S. Cox, M.S. Ridout, B.J.T. Morgan, M.F. Tuite, The number and transmission of [psi+] prion seeds (propagons) in the yeast saccharomyces cerevisiae, PLoS ONE 4 (3) (2009) 1–10.
[12] D.A. Charlebois, G. Balázsi, Modeling cell population dynamics, In Silico Biol. 13 (1–2) (2019) 21–39.
[13] A. Ciechanover, Y.T. Kwon, Protein quality control by molecular chaperones in neurodegeneration, Front. Neurosci. 11 (2017) 185.
[14] W. Commons, Saccharomyces cerevisiae cells in dic microscopy, 2010, File: S_cerevisiae_under_DIC_microscopy.jpg.
[15] N.A. Cookson, S.W. Cookson, L.S. Tsimring, J. Hasty, Cell cycle-dependent variations in protein concentration, Nucleic Acids Res. 38 (8) (2010) 2676–2681.
[16] B. Cox, F. Ness, M. Tuite, Analysis of the generation and segregation of propagons: entities that propagate the $[PSI^+]$ prion in yeast, Genetics 165 (1) (2003) 23–33.
[17] B. Cox, M. Tuite, The life of [psi], Curr. Genet. (2017) 1–8.
[18] L. Dagum, R. Menon, Openmp: an industry-standard api for shared-memory programming, IEEE Comput. Sci. Eng. 5 (1) (Jan. 1998) 46–55.
[19] T.S.G. Database, Sup35 / ydr172w overview, https://www.yeastgenome.org/locus/S000002579.
[20] J.K. Davis, S.S. Sindi, A study in nucleated polymerization models of protein aggregation, Appl. Math. Lett. 40 (2015) 97–101.
[21] A. Derdowski, S. Sindi, C. Klaips, S. DiSalvo, T. Serio, A size threshold limits prion transmission and establishes phenotypic diversity, Science 330 (6004) (2010) 680–683.
[22] E. Gaburro, M. Dumbser, M.J. Castro, Direct arbitrary-Lagrangian-Eulerian finite volume schemes on moving nonconforming unstructured meshes, Comput. Fluids 159 (2017) 254–275.
[23] A. Guittet, M. Theillard, F. Gibou, A stable projection method for the incompressible Navier–Stokes equations on arbitrary geometries and adaptive quad/octrees, J. Comput. Phys. 292 (2015) 215–238.
[24] Y. Guyot, F. Luyten, J. Schrooten, I. Papantoniou, L. Geris, A three-dimensional computational fluid dynamics model of shear stress distribution during neotissue growth in a perfusion bioreactor, Biotechnol. Bioeng. 112 (12) (2015) 2591–2600.
[25] Y. Guyot, I. Papantoniou, F.P. Luyten, L. Geris, Coupling curvature-dependent and shear stress-stimulated neotissue growth in dynamic bioreactor cultures: a 3d computational model of a complete scaffold, Biomech. Model. Mechanobiol. 15 (1) (Feb 2016) 169–180.
[26] D. Hall, H. Edskes, Computational modeling of the relationship between amyloid and disease, Biophys. Rev. 4 (3) (2012) 205–222.
[27] C. Hatzis, D. Porro, Morphologically-structured models of growing budding yeast populations, J. Biotechnol. 124 (2) (2006) 420–438.

[28] S. Hross, J. Hasenauer, Analysis of cfse time-series data using division-, age- and label-structured population models, Bioinformatics 32 (15) (2016) 2321–2329.
[29] E. Javierre, F.J. Vermolen, C. Vuik, S. van der Zwaag, A mathematical analysis of physiological and morphological aspects of wound closure, J. Math. Biol. 59 (5) (Nov 2009) 605–630.
[30] D. Kaganovich, R.R. Kopito, J. Frydman, Misfolded proteins partition between two distinct quality control compartments, Nature 454 (2008) 1088–1095.
[31] A. Kinkhabwala, A. Khmelinskii, M. Knop, Analytical model for macromolecular partitioning during yeast cell division, BMC Biophys. 7 (1) (Sep 2014) 10.
[32] P. Lantos, From slow virus to prion: a review of transmissible spongiform encephalopathies, Histopathology 20 (1) (1992) 1–11.
[33] F. Losasso, F. Gibou, R. Fedkiw, Simulating water and smoke with an octree data structure, ACM Trans. Graph. (SIGGRAPH Proc.) (2004) 457–462.
[34] P. Macklin, J. Lowengrub, An improved geometry-aware curvature discretization for level set methods: application to tumor growth, J. Comput. Phys. 215 (2) (2006) 392–401.
[35] J.D. Marth, A unified vision of the building blocks of life, Nat. Cell Biol. 10 (9) (2008) 1015.
[36] S. Mazumder, Numerical Methods for Partial Differential Equations: Finite Difference and Finite Volume Methods, Academic Press, 2015.
[37] R. Milo, R. Phillips, N. Orme, Cell Biology by The Numbers, Garland Science, 2015.
[38] C. Min, F. Gibou, Geometric integration over irregular domains with application to level-set methods, J. Comput. Phys. 226 (2) (Oct. 2007) 1432–1443.
[39] C. Min, F. Gibou, A second order accurate level set method on non-graded adaptive Cartesian grids, J. Comput. Phys. 225 (2007) 300–321.
[40] M. Mirzadeh, M. Theillard, A. Helgadöttir, D. Boy, F. Gibou, An adaptive, finite difference solver for the nonlinear Poisson-Boltzmann equation with applications to biomolecular computations, Commun. Comput. Phys. 13 (1) (2013) 150–173.
[41] J.D. Murray, Mathematical Biology II: Spatial Models and Biomedical Applications, vol. 3, Springer-Verlag, 2001.
[42] J.D. Murray, Mathematical Biology: I. An Introduction, vol. 17, Springer Science & Business Media, 2007.
[43] G.A. Newby, S. Lindquist, Blessings in disguise: biological benefits of prion-like mechanisms, Trends Cell Biol. 23 (6) (2013) 251–259.
[44] N.I. of Health, Creutzfeldt-Jakob disease fact sheet, 2018.
[45] M. Ogrodnik, H. Salmonowicz, R. Brown, J. Turkowska, W. Średniawa, S. Pattabiraman, T. Amen, A.-c. Abraham, N. Eichler, R. Lyakhovetsky, D. Kaganovich, Dynamic junq inclusion bodies are asymmetrically inherited in mammalian cell lines through the asymmetric partitioning of Vimentin, Proc. Natl. Acad. Sci. USA 111 (22) (Jun 2014) 8049–8054, PMID: 24843142.
[46] OpenMP Architecture Review Board, OpenMP application program interface version 5.0, May 2018.
[47] S. Osher, R. Fedkiw, Level Set Methods and Dynamic Implicit Surfaces, Springer-Verlag, New York, NY, 2002.
[48] E.M. Rutter, T.L. Stepien, B.J. Anderies, J.D. Plasencia, E.C. Woolf, A.C. Scheck, G.H. Turner, Q. Liu, D. Frakes, V. Kodibagkar, et al., Mathematical analysis of glioma growth in a murine model, Sci. Rep. 7 (1) (2017) 1–16.
[49] S.S. Sindi, Mathematical modeling of prion disease, InTechOpen 03 (2017).
[50] B. Sampaio-Marques, W.C. Burhans, P. Ludovico, Yeast at the forefront of research on ageing and age-related diseases, in: Yeasts in Biotechnology and Human Health, 2019, pp. 217–242.
[51] P. Satpute-Krishnan, S.X. Langseth, T.R. Serio, Hsp104-dependent remodeling of prion complexes mediates protein-only inheritance, PLoS Biol. 5 (2) (2007) e24.
[52] J.A. Sethian, Level Set Methods and Fast Marching Methods, Cambridge University Press, Cambridge, 1999.
[53] S. Sindi, F. Santiago, K. Flores, Numerical approaches to division and label structured population models, Lett. Biomath. 7 (1) (2020) 153–170.
[54] M. Sussman, K.M. Smith, M. Hussaini, M. Ohta, Z.-W. Rong, A sharp interface method for incompressible two-phase flows, J. Comput. Phys. 221 (2007) 469–505.
[55] M. Tanaka, S.R. Collins, B.H. Toyama, J.S. Weissman, The physical basis of how prion conformations determine strain phenotypes, Nature 442 (7102) (2006) 585–589.
[56] M. Theillard, A volume-preserving reference map method for the level set representation, J. Comput. Phys. 442 (2021) 110478.
[57] M. Theillard, L.F. Djodom, J.-L. Vié, F. Gibou, A second-order sharp numerical method for solving the linear elasticity equations on irregular domains and adaptive grids–application to shape optimization, J. Comput. Phys. 233 (2013) 430–448.
[58] M. Theillard, F. Gibou, T. Pollock, A sharp computational method for the simulation of the solidification of binary alloys, J. Sci. Comput. 63 (2) (2015) 330–354.
[59] M. Theillard, F. Gibou, D. Saintillan, Sharp numerical simulation of incompressible two-phase flows, J. Comput. Phys. 391 (2019) 91–118.
[60] M. Theillard, C. Rycroft, F. Gibou, A multigrid method on non-graded adaptive octree and quadtree Cartesian grids, J. Sci. Comput. 55 (2013) 1–15.
[61] M. Theillard, D. Saintillan, Computational mean-field modeling of confined active fluids, J. Comput. Phys. 397 (2019) 108841.
[62] M.F. Tuite, T.R. Serio, The prion hypothesis: from biological anomaly to basic regulatory mechanism, Nat. Rev. Mol. Cell Biol. 11 (12) (2010) 823–833.
[63] C.B. Tyson, P.G. Lord, A.E. Wheals, Dependency of size of saccharomyces cerevisiae cells on growth rate, J. Bacteriol. 138 (1) (1979) 92–98.
[64] F. Vermolen, M.W.G. van Rossum, E.J. Perez, J. Adam, Modeling of Self Healing of Skin Tissue, Springer, Netherlands, Dordrecht, 2007, pp. 337–363.
[65] J. Villali, J. Dark, T.M. Brechtel, F. Pei, S.S. Sindi, T.R. Serio, Nucleation seed size determines amyloid clearance and establishes a barrier to prion appearance in yeast, Nat. Struct. Mol. Biol. 27 (6) (2020) 540–549.
[66] R. Wang, A. Kamgoue, C. Normand, I. Léger-Silvestre, T. Mangeat, O. Gadal, High resolution microscopy reveals the nuclear shape of budding yeast during cell cycle and in various biological states, J. Cell Sci. 129 (24) (2016) 4480–4495.
[67] S. Wise, J. Lowengrub, H. Frieboes, V. Cristini, Three-dimensional multispecies nonlinear tumor growth—I: model and numerical method, J. Theor. Biol. 253 (3) (2008) 524–543.
[68] J. Yang, M.A. McCormick, J. Zheng, Z. Xie, M. Tsuchiya, S. Tsuchiyama, H. El-Samad, Q. Ouyang, M. Kaeberlein, B.K. Kennedy, et al., Systematic analysis of asymmetric partitioning of yeast proteome between mother and daughter cells reveals “aging factors” and mechanism of lifespan asymmetry, Proc. Natl. Acad. Sci. 112 (38) (2015) 11977–11982.
[69] L. Yang, J.C. Effler, B.L. Kutscher, S.E. Sullivan, D.N. Robinson, P.A. Iglesias, Modeling cellular deformations using the level set formalism, BMC Syst. Biol. 2 (Jul 2008) 68, PMID: 18652669.